RESEARCH ARTICLE

NANO · MICRO small
www.small-journal.com

Shape Memory Polymers with Rapid Multi-Solvent Responsiveness for Dual-Mode Vapor Sensing

Qiong Zuo, Lingyu Zhao, Zengbai Ouyang, Jiaxin Guo, Yongzhi Liang, and Jinsong Leng**

Solvent-responsive shape memory polymers (SR-SMPs) are smart materials that can retain their original shape when exposed to solvents. However, most reported SR-SMPs show slow shape recovery and lack multi-solvent responsiveness, which greatly limits their practical use. Here, a novel SR-SMP is introduced by creating a dual-component network comprising aliphatic polyurethane acrylate (AUA) and polystyrene-block-polyisoprene-block-polystyrene (SIS). The AUA phase provides mechanical stability and prevents excessive swelling, while the SIS phase, compatible with low-polarity solvents, promotes plasticization and speeds up shape recovery. This results in excellent shape memory performance when exposed to various solvents. The incorporation of carbon nanotubes (CNTs) and carbon black (CB) further accelerates shape recovery to about 20 s, which is over an order of magnitude faster than previously reported SR-SMPs. Based on these properties, a dual-mode sensor is developed using the SR-SMP, capable of providing both visual and electrical responses when exposed to petroleum ether vapor. The visual shape change offers an intuitive indication, while the electrical signal delivers a more accurate output, with a detection limit of 0.013 g·L^{-1} and a sensitivity of 1519.8 L·g^{-1}. The as-developed SR-SMP exhibits great promise in the creation of next-generation solvent-driven smart materials.

1. Introduction

Shape-memory polymers (SMPs) are stimuli-responsive materials capable of recovering programmed configurations upon exposure to stimuli, including heat, light, or chemicals.[1–5] Their unique combination of tunable stiffness, reconfigurability, and processability enables diverse applications across aerospace, biomedical engineering, flexible electronics, soft robotics, and 4D printing.[6–8] While most research has focused on thermally-activated SMPs, solvent-responsive systems (SR-SMPs) represent an energy-efficient and convenient alternative that enables shape programming through solvent exposure, eliminating the need for heating.[9–11] Current SR-SMP development has predominantly emphasized aqueous systems, driven by demands in biomedical and green chemistry applications, as well as the design simplicity afforded by water's polarity and the ease of incorporating hydrogen-bonding functional groups.[12,13] Yet organic solvent-responsive SMPs represent another promising direction for expanding SR-SMP applications into the chemical, petroleum, and pharmaceutical sectors. Despite the advancements, existing SR-SMPs face two critical limitations: 1) narrow solvent responsiveness, typically restricted to one or two specific solvents,[14] and 2) slow recovery kinetics, often requiring hours to complete.[15]

For an ideal SR-SMP, fast recovery behavior and structural stability during solvent exposure are essential.These two requirements often conflict because improving solvent interaction to speed up response usually weakens network integrity through excessive swelling, while strengthening mechanical stability can block solvent diffusion and slow down recovery.[16] In this work, we developed a dual-component SR-SMP (AUA-SIS) to resolve the intrinsic conflict between structural stability and rapid solvent responsiveness by decoupling these functions into distinct network domains. The material integrates a rigid AUA network to provide mechanical robustness and act as a diffusion barrier, effectively limiting excessive swelling and preserving the programmed shape. The SIS was selected as the soft phase whose solubility parameters closely match those of low-polarity solvents such as petroleum ether and hexane.[17,18] This compatibility guided by thermodynamic principles, enables rapid solvent uptake and efficient plasticization of the soft phase. The synergistic combination of AUA and SIS enables fast, reversible shape recovery and broad solvent responsiveness in low-polarity environments. CNTs and CB were further incorporated into the AUA-SIS, which could weaken the intermolecular interactions between long polymer chains, in turn facilitating solvent diffusion into the network and accelerating shape recovery. The composite exhibited a significantly

Q. Zuo, L. Zhao, Z. Ouyang, J. Guo, Y. Liang
Department of Materials Science and Engineering
Southern University of Science and Technology
Shenzhen 518055, China
E-mail: zhaoly@sustech.edu.cn

J. Leng
Center for Composite Materials and Structures
Harbin Institute of Technology
Harbin 150080, China
E-mail: lengjs@hit.edu.cn

The ORCID identification number(s) for the author(s) of this article can be found under https://doi.org/10.1002/smll.202509216

DOI: 10.1002/smll.202509216

accelerated shape recovery rate, achieving a response time of about 20 s, which is an order of magnitude faster compared to most previous studies.[7,19]

Beyond its responsiveness to liquid solvents, the SIS segment, thermodynamically compatible with low-polarity solvents, also enables the material with solvent vapor-responsive behavior. Due to its strong affinity for low-polarity gas molecules, the chain segment of SIS undergoes rapid relaxation, enabling visible shape change upon vapor exposure. The incorporation of conductive fillers imparts the material with strain-sensitive electrical properties, allowing solvent-induced deformation to be translated into measurable electrical signals. Leveraging these properties, we developed a dual-mode sensor for volatile solvents based on the SR-SMP. The sensor enables qualitative detection through visible macroscopic shape changes and provides electrical signal outputs that reflect the presence and concentration of solvent vapor, achieving a detection limit of as low as 0.013 $g \cdot L^{-1}$ and a maximum sensitivity of 1519.8 $L \cdot g^{-1}$. These results underscore the versatility and application potential of the composite as a high-performance solvent-responsive material, highlighting its broad prospects in areas such as environmental monitoring and smart actuators.

2. Results and Discussion

2.1. Design of AUA-SIS

We developed the SR-SMP (AUA–SIS) using a rational dual-component network design. AUA acts as a rigid, cross-linkable scaffold, resisting solvent-induced deformation and providing mechanical stability. SIS contains low-polarity, flexible chain segments that enable strong molecular interactions with low-polarity solvents because of their closely matched solubility parameters. This facilitates rapid solvent diffusion and chain mobility when stimulated. UV-initiated photopolymerization with TPO as the photoinitiator allows covalent cross-linking between AUA and SIS (**Figure** 1a), creating a network structure where each component serves a distinct functional role (Figure 1b). This structural design renders the SR-SMP with excellent shape-memory properties and mechanical performance, allowing it to recover to its original shape through either solvent immersion or vapor exposure (Figure 1c). This solvent vapor response is primarily caused by the SIS segments, whose low-polarity and flexible chains enable effective interaction with solvent molecules in the gas phase, enhancing chain mobility for shape recovery.

2.2. Shape Memory Properties of the AUA-SIS

The composition of AUA and SIS plays a crucial role in determining both the mechanical properties and shape-memory performance of the SR-SMP.[20] The FTIR spectra in **Figure** 2a present the chemical transformations of AUA and SIS before and after UV irradiation. The spectrum of the original AUA material reveals a distinct C═C stretching vibration peak at 1633 cm^{-1}, while the SIS spectrum displays a characteristic bending vibration peak at 806 cm^{-1}, indicating the presence of unreacted double bonds in the polymer precursors. UV exposure leads to a significant attenuation of the C═C stretching vibration, evidencing the phototriggered bond conversion and formation of a stable cross-linked structure.

We examine samples with AUA: SIS ratios of 1:1, 1:2, and 1:4. The stress–strain curves at room temperature (Figure 2b) reveal that increasing the SIS content reduces Young's modulus while enhancing elongation at break (Figure 2c), consistent with the intrinsic mechanical properties observed in the AUA-only (1:0) and SIS-only (0:1) samples. Besides, neither of these single-component polymers exhibits shape-memory behavior. This behavior can be attributed to the increased concentration of flexible chain segments that enhance polymer chain mobility.[21] Dynamic mechanical analysis (DMA) further supports these findings. As shown in Figure 2d, a continuous decline in storage modulus is observed with increasing SIS content. The Tan Delta curves (Figure 2e) exhibit two distinct peaks, corresponding to the segmental relaxations of SIS and AUA domains. The low-temperature peak reflects the glass transition of the SIS-rich phase and is closely related to the shape recovery process, serving as the switching temperature (T_w) of the AUA-SIS. The cross-linked structure forms a continuous network, remains functionally distinct yet structurally integrated. This structure enables SIS to impart dynamic flexibility, while AUA maintains mechanical stability, ensuring reversible shape-memory behavior. As shown in **Table** 1, the sample with a 1:2 ratio exhibits balanced shape-memory performance, achieving a shape fixity ratio (R_f) of 95.9% and a shape recovery ratio (R_r) of 97.8%. The thermal shape-memory cycle further confirms this optimal performance, demonstrating both excellent shape fixity and rapid recovery (Figure 2f; Figure S1, Supporting Information). The deformed AUA-SIS film was deformed at 90 °C and fixed at room temperature (Movies S1 and S2, Supporting Information). The solvent-response shape recovery behavior was examined in a low-polarity solvent (petroleum ether) (Figure 2g), and the recovery process was completed within ≈30 s (Movies S3 and S4, Supporting Information). When exposed to petroleum ether, the deformed AUA-SIS gradually recovers its original shape over time, primarily due to the plasticizing effect of the solvent. This behavior is governed by the material's solubility and the molecular interactions between the polymer and solvent.[22,23] From a thermodynamic perspective, the solubility parameter of petroleum ether is close to that of SIS, favoring molecular compatibility and facilitating solvent penetration into the polymer. At the molecular level, the swelling behavior was further analyzed using the Korsmeyer–Peppas model ($\frac{M_t}{M_1} = kt^n$) in the early-time regime (Figure S2, Supporting Information), where $\frac{M_t}{M_1}$ is the fractional solvent uptake at time t, k is a kinetic constant, and n is the diffusion exponent that reflects the transport mechanism.[24] For petroleum ether, the data fit this model well, yielding $n = 0.71$ with high correlation ($R^2 = 0.991$). This value indicates anomalous swelling, where petroleum ether molecules diffuse into the SIS domains and disrupt intermolecular interactions. These effects enhance segmental mobility and gradually lower T_w. Once T_w falls below ambient temperature, the polymer chains regain flexibility, allowing the material to restore its original shape. This behavior is intrinsically linked to the thermal shape recovery effect, the basis of solvent-induced responsiveness. Solvent absorption weakens intermolecular interactions between polymer chains, effectively lowering the T_w

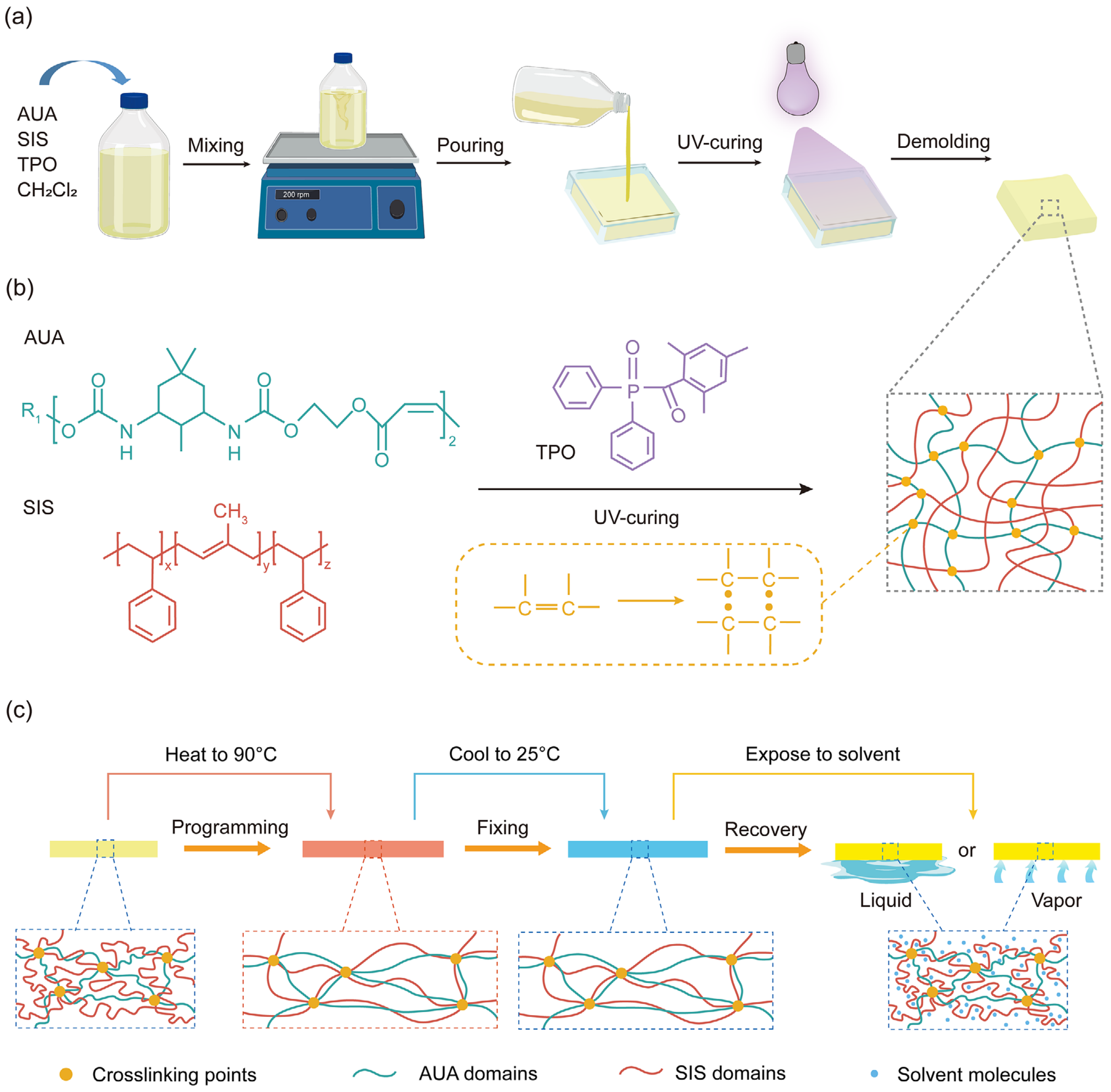

Figure 1. The preparation and mechanism of the AUA-SIS. a) Schematic illustration of the preparation process of AUA-SIS. b) Chemical structure of AUA and SIS and their cross-linking reaction under UV exposure, forming a polymer network with permanent phases (AUA domains), cross-linking points, and reversible switching phase (SIS domains). c) Mechanism of shape-memory behavior, including recovery through the activation of liquid-phase or vapor-phase solvent. All symbols are defined in the figure.

below room temperature. This facilitates chain segment mobility and induces shape recovery, similar to direct thermal activation by raising the temperature above T_w. The AUA-SIS demonstrates shape recovery not only in response to liquid solvent but also to solvent vapor (Figure 2g), with the vapor concentration about 2 g·L^{-1}, a phenomenon rarely reported in the literature. Exposure to solvent vapor leads to a complete recovery of the deformed film, indicating that the AUA-SIS can effectively respond to indirect solvent exposure without direct immersion (Movies S5 and S6, Supporting Information). This behavior highlights the material's capability in reacting to versatile environmental stimuli.

2.3. The Selection of Fillers for Composite AUA-SIS

CNTs/CB@AUA-SIS was prepared by introducing CNTs and CB into the AUA-SIS matrix with the ratio of 1:2, which exhibits

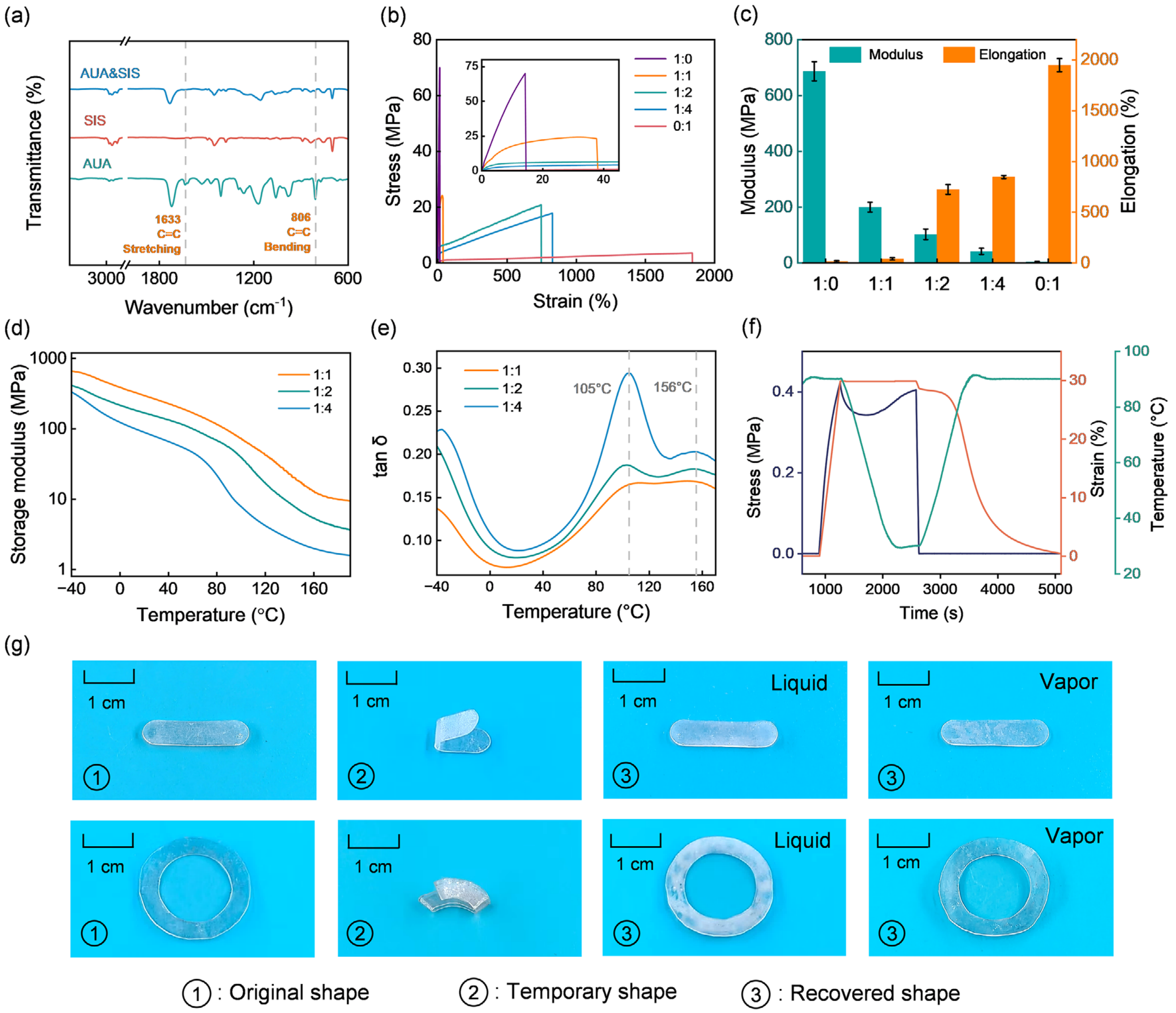

Figure 2. The shape memory properties of the AUA-SIS. a) FTIR spectra of the AUA and SIS before and after UV polymerization. b) Stress–strain curves and c) Modulus and elongation of AUA-SIS with different component ratios (1:0, 1:1, 1:2, 1:4, and 0:1). The error bars show the s.d. values for the results from three samples. d) Storage modulus and e) Tan Delta curves of the AUA-SIS obtained by DMA. f) Shape memory curves of the AUA-SIS with the ratio of 1:2. g) Photographs of the shape-memory behavior of AUA-SIS with different deformations in response to petroleum ether liquid or vapor.

optimal shape-memoryperformance. The addition of CB led to a notable improvement in mechanical ductility, as evidenced by a significant increase in elongation at break (**Figure 3**a; Figure S3, Supporting Information). The enhanced deformability extends the strain range for shape programming, which is critical for shape memory polymer applications. After doping with both CNT and CB, the electrical and thermal conductivities were both improved compared to CNT-only samples (Figure 3b,c). This enhancement is attributed to the synergistic interaction between CNTs and CB, with CNTs forming a continuous network and CB serving as a bridging agent that reinforces both electrical and thermal pathways.[25,26] With the increase of CNT content, the thermal stability of the polymer matrix remained unaffected (Figure 3d), while dynamic mechanical analysis (Figure 3e) showed a shift in the low-temperature peak, indicating improved chain mobility. This behavior is likely due to disrupted intermolecular interactions between polymer chains caused by the presence of nanofillers.[27–29] The high-temperature transition stayed stable, suggesting the structural integrity of the hard

Table 1. Shape fixity ratio (R_f) and Shape recovery ratio (R_r) of AUA-SIS with different proportion conditions.

	1:1	1:2	1:4
Shape fixity ratio (R_f)	93.4%	95.9%	87.3%
Shape recovery ratio (R_r)	12.1%	97.8%	73.3%

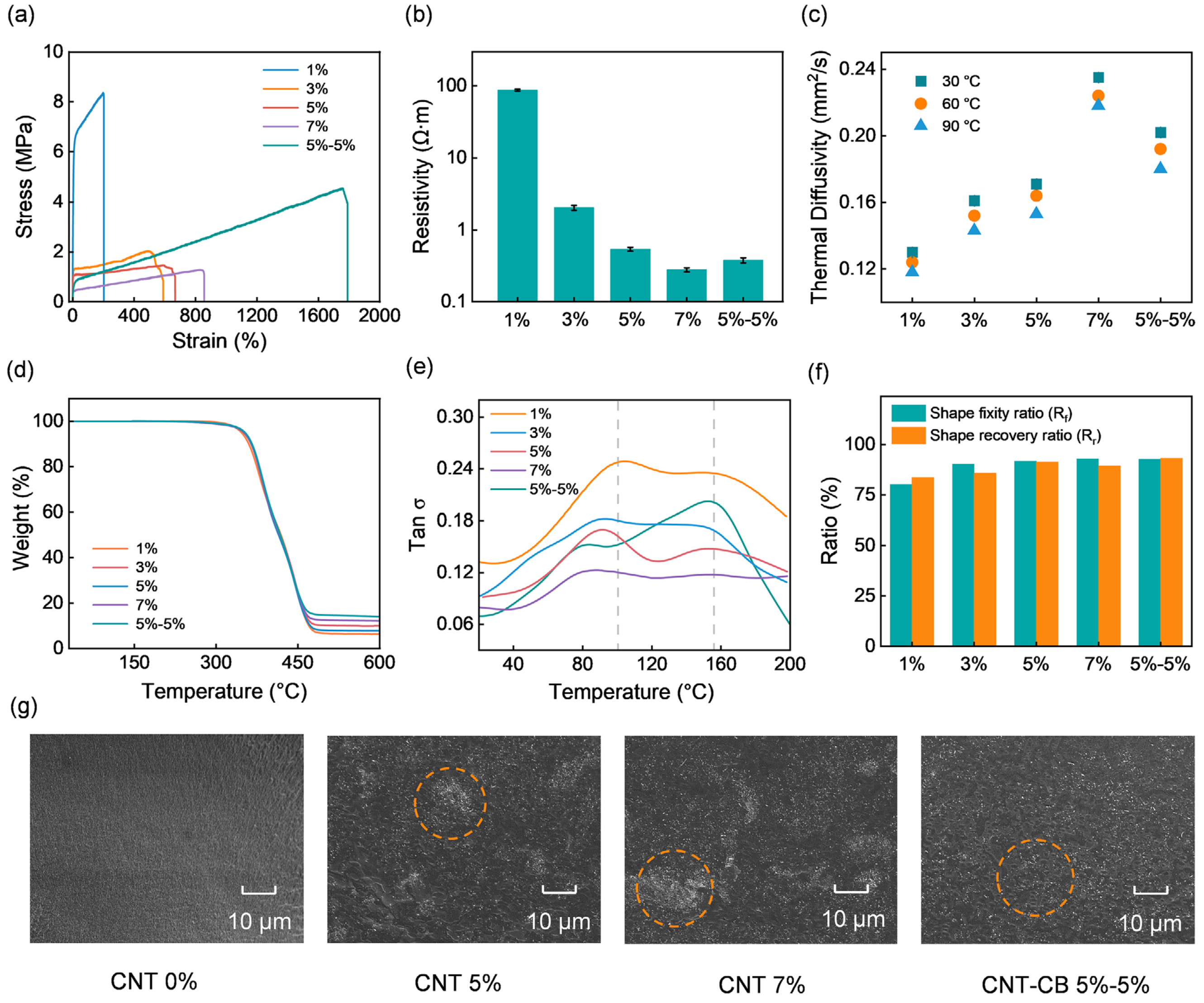

Figure 3. The characterization of the AUA-SIS composite with varying CNT and CB content. a) Tensile stress-strain curves, b) Electrical resistivity, c) Thermal diffusivity, d) TGA, and e) Tan Delta curves of AUA-SIS composites with different filler contents. The error bars show the s.d. values for the results from three samples. f) Shape fixity and recovery performance as assessed from shape memory tests. g) SEM images of AUA-SIS composites.

phase was preserved. The SEM images further revealed that the introduction of CB effectively suppressed CNT agglomeration and promoted a more uniform distribution of fillers within the matrix (Figure 3g). This combination of phase stability and improved network morphology contributes to the improved shape memory performance of the CNTs/CB@AUA-SIS (Figure 3f).

2.4. Shape Memory Properties of CNTs/CB@AUA-SIS

The CNTs/CB@AUA-SIS exhibit enhanced responsivity under solvent-triggered conditions. As shown in **Figure** 4a, we subjected the SR-SMP to various deformations in petroleum ether, including torsion, stretching, and bending at angles of 60°, 120°, and 180°, and recorded the corresponding recovery time. The results indicate that CNTs/CB@AUA-SIS maintain excellent shape recovery capabilities under these deformation conditions. Both AUA-SIS and CNTs/CB@AUA-SIS exhibited effective shape recovery in low-polarity solvents, such as petroleum ether (Figure 4b), n-pentane (Figure S4, Supporting Information), n-hexane (Figure S5, Supporting Information), and cyclohexane (Figure S6, Supporting Information). This broad solvent responsiveness stems from the similar solubility principles, enabling the soft segments of the material to interact with and absorb a variety of low-polarity liquids, promoting swelling and softening, which facilitates shape recovery (Figure 4c). A particularly significant observation is that under the same fixation conditions (Movies S1 and S7, Supporting Information), the solvent-responsive shape recovery time of CNTs/CB@AUA-SIS was shorter than that of AUA-SIS (Movies S3, S8, and Figure S7, Supporting Information), suggesting an enhancement in recovery efficiency. This shape recovery property of the composite SMP

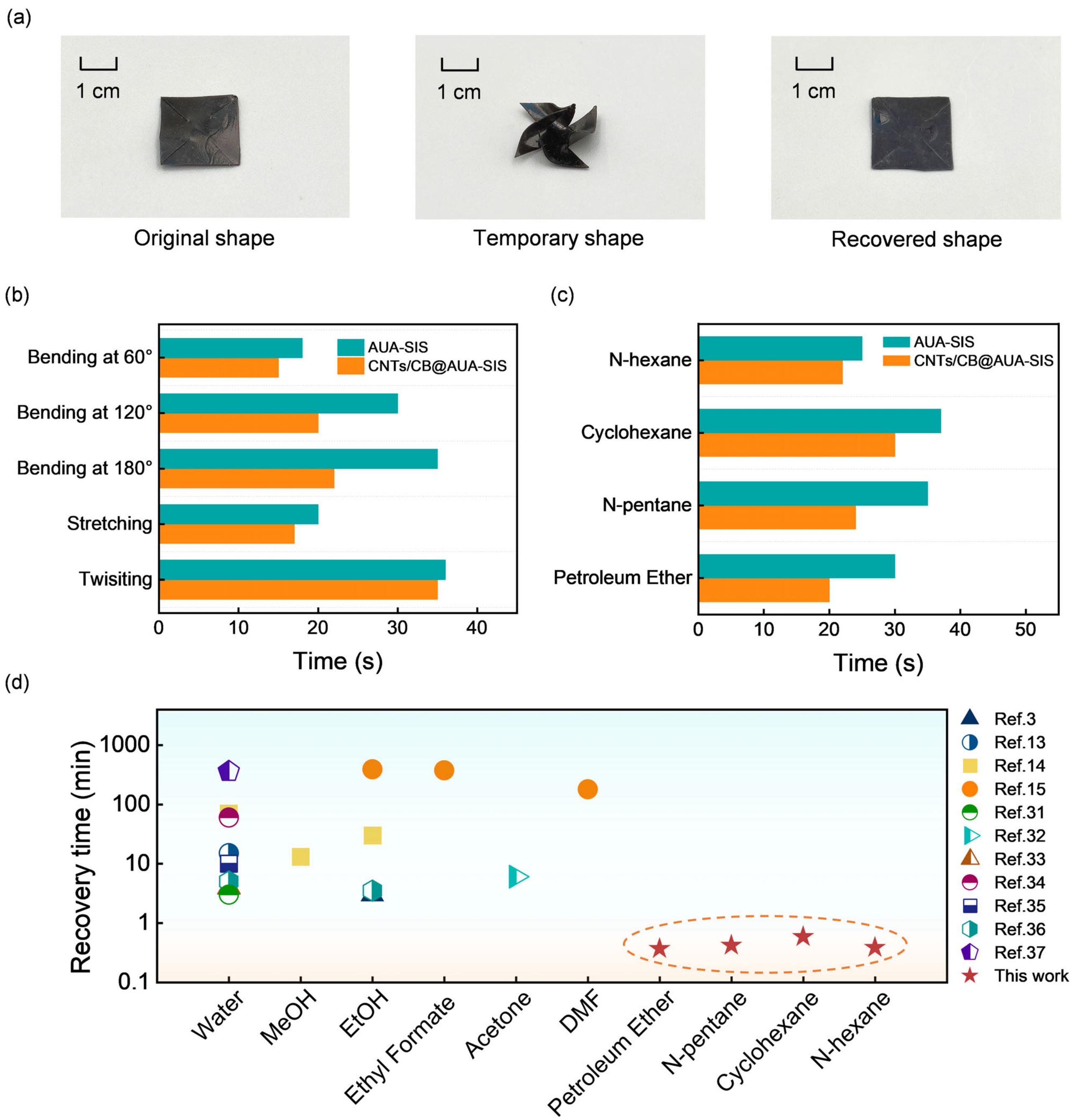

Figure 4. The enhanced solvent-responsive shape memory effect of CNTs/CB@AUA-SIS. a) Photographs of the shape recovery process of CNTs/CB@AUA-SIS in petroleum ether. Comparison of recovery time for AUA-SIS and CNTs/CB@AUA-SIS b) under different deformations (twisting, stretching, and bending at 60°, 120°, and 180°) in petroleum ether and c) upon the contact of various solvents (n-hexane, cyclohexane, n-pentane, and petroleum ether). d) Comparison of the solvent types and shape recovery time of SR-SMP in previous reports and this work.

upon exposure to solvent vapor conditions was confirmed in Movie S9 and Figure S8 (Supporting Information). This improvement is mainly due to conductive fillers, which reduce intermolecular forces and facilitate softening in solvent environments.[30] Compared to previously reported polymers, CNTs/CB@AUA-SIS respond to multiple solvents (Table S1, Supporting Information). It also reduces the response time from tens of minutes to about 20 s, exhibiting exceptional solvent-responsive shape memory recovery performance (Figure 4d).[3,13–15,31–37]

Different solvents exhibited varying effects on shape recovery, which can be explained using solubility parameter theory and the Scatchard-Hildebrand equation:[38]

$$\Delta H_m = \phi_1 \phi_2 V_m \left(\delta_1 - \delta_2\right)^2 \tag{1}$$

where δ_1 and δ_2 represent the solubility parameters of the solvent and polymer, respectively. Φ_1 and Φ_2 represent the volume fractions of the polymer and solvent, respectively. V_m is the molar volume of the mixture, and ΔH_m denotes the enthalpy change associated with mixing. According to Equation 1, the smaller the difference (δ_1-δ_2), the lower the mixing enthalpy (ΔH_m), indicating better compatibility and greater miscibility between the polymer and solvent. This enhanced miscibility leads to improved polymer swelling, which in turn facilitates chain relaxation and accelerates the shape recovery process. Experimental data further support this correlation. Solvents such as petroleum ether (14.9–15.6 $MPa^{1/2}$), which have solubility parameters closer to that of the material (15.3 $MPa^{1/2}$), exhibited shorter recovery time due to improved plasticization and accelerated chain relaxation. Compared to other solvents, cyclohexane has lower compatibility (16.8 $MPa^{1/2}$) and a larger molecular weight, which hinders the solvent's penetration into the polymer chains, collectively leading to a slower recovery rate. These findings underscore the critical role of solvent-polymer interactions in governing shape memory behavior.

2.5. Dual-Mode Vapor Sensor Based on CNTs/CB@AUA-SIS

A dual-mode sensor system was fabricated based on the solvent sensitivity of CNTs/CB@AUA-SIS, as shown in **Figure** 5a. This system utilizes the shape memory effect and piezoresistivity of the composite, enabling it to respond to petroleum ether vapor through simultaneous visible macroscopic deformation and resistance variation. Upon exposure to organic vapor, solvent molecules penetrate the polymer matrix, interacting with polymer chains and inducing segmental relaxation and volumetric swelling.[39,40] This swelling increases the interparticle distance between CNTs, disrupting the percolated conductive network and leading to an increase in electrical resistance. The shape memory effect further amplifies this process by enhancing chain migration during shape recovery, triggered by solvent exposure, thereby boosting the material's electrical sensitivity (Figure 5b). This highlights the advantage of solvent-responsive behavior. Owing to the material's sensitivity to solvent molecules, the sensor is capable of detecting ultra-low concentrations of petroleum ether vapor (0.013 $g \cdot L^{-1}$), which corresponds to the lowest concentration at which a discernible resistance change was observed, demonstrating its effectiveness in organic vapor detection (Figure 5c). A correlation between vapor concentration and resistance change was established (Figure 5d), revealing a high sensitivity of 1519.8 $L \cdot g^{-1}$, calculated as the linear fit between the relative resistance change ($\Delta R/R$) and vapor concentration under low-concentration conditions. As the vapor concentration increases, the sensor's resistance exhibits a corresponding rise, indicating that more solvent molecules penetrate the polymer network and accelerate the process of chain relaxation (Figure 5e).

The sensor exhibited significant and reversible resistance changes upon repeated exposure to petroleum ether vapor, while it gradually returned to its baseline level in the air (Figure 5f). Since vapor-triggered recovery is relatively slow and the macroscopic deformation under our short exposure was negligible, reprogramming was unnecessary in this test. This reversible behavior demonstrates its reliability and reusability for detecting dynamic changes in organic vapor concentrations. It is worth emphasizing that the sensor's macroscopic shape transformation serves as an additional indicator of solvent exposure (Figure 5g). As the solvent-induced recovery progressed, the shape of the predeformed material gradually returned to its original configuration, accompanied by a corresponding increase in electrical resistance. The sensor exhibited stable resistance output over more than 50 solvent vapor cycles (Figure S9, Supporting Information), confirming its cyclic durability and long-term applicability. This visual shape recovery, coupled with real-time resistance variation, demonstrates the dual-output capability of the sensor.

3. Conclusion

In conclusion, we have successfully developed a novel SR-SMP based on a co-polymer of AUA and SIS. This material exhibits a rapid shape recovery response to multiple solvents, and even upon exposure to the corresponding solvent vapor. The incorporation of CNT and CB fillers enhances the solvent responsiveness of AUA-SIS by improving chain mobility and interaction with vapor molecules, resulting in a response time of 20 s, 1 order of magnitude faster than the state-of-the-art reported SR-SMPs. The conductive network formed by the fillers enables sensing functionality, enabling the detection of trace organic vapors such as petroleum ether. The vapor sensor based on the SR-SMP is capable of detecting ultra-low concentrations of petroleum ether vapor (0.013 $g \cdot L^{-1}$) and exhibits highly repeatable, high-sensitivity responses (1519.8 $L \cdot g^{-1}$), underscoring its potential for monitoring in dynamic vapor environments. In addition to its electrical responsiveness, the sensor simultaneously provides macroscopic visual feedback through shape recovery, demonstrating a dual-modal output in both electrical and visual domains. These findings demonstrate the excellent performance of the SR-SMP and highlight its promising potential for broader applications in intelligent material systems.

4. Experimental Section

Material: Aliphatic polyrethane acrylate (AUA, viscosity = 65–85 Pa •s (25 °C)) was provided by Shanghai Titan Technology Co., Ltd. Polystyrene-block-polyisoprene-block-polystyrene (SIS, purity ≥ 99%) was obtained from Guangzhou Xiaofan Technology Co., Ltd. 2,4,6-trimethylbenzoyldiphenyl phosphine oxide (TPO) was provided by Shanghai Macklin Biochemical Technology Co., Ltd. Multi-wall carbon nanotubes (WMCNT, purity ≥ 99%, length = 10–30 µm, diameter = 10–20 nm) and carbon black (CB, diameter = 30–45 nm) were purchased from Nanjing XFNANO Materials Tech Co., Ltd. Dichloromethane (CH_2Cl_2, purity ≥ 99.5%) was obtained from Guangzhou ChemMole Biotechnology Co., Ltd. Petroleum ether (Boiling point = 60–90 °C), N-hexane (purity ≥ 98%), Cyclohexane (purity ≥ 99.5%) and N-pentane (purity ≥99%) was provided by Shanghai Aladdin Biochemical Technology Co., Ltd; Deionized water was used in all experiments. All the chemicals were of analytical grade and used without further purification.

Sample Preparation and Synthesis of the Nanocomposites: In this study, AUA (1 g) and SIS (2 g) were first dissolved in CH_2Cl_2 (15 g) and blended with a 2 wt.% concentration of TPO (0.06 g) as an initiator. This mixture was thoroughly stirred in the dark for 12 h to ensure homogeneity. Subsequently, the resultant solution was poured into a transparent vessel and subjected to UV light at 395 nm for 30 min to induce curing.

For the doping of the SR-SMP, conductive materials (WMCNTs and CB) were incorporated into the aforementioned homogeneous solution. The

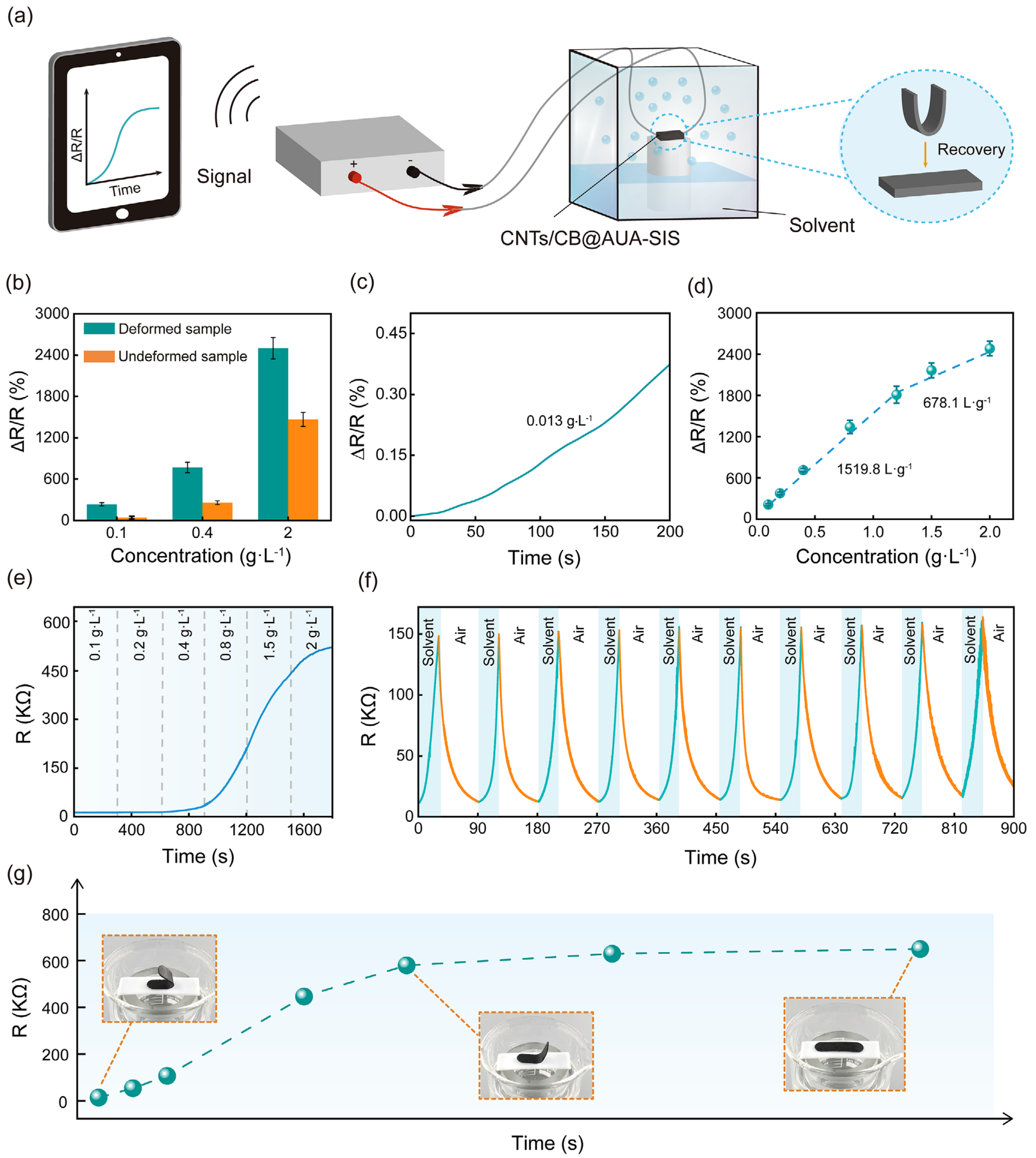

Figure 5. The sensing capabilities of the dual-modal sensor for organic solvent vapor detection. a) Schematic representation of the CNTs/CB@AUA-SIS based sensor system for detecting petroleum ether vapor concentrations. b) Comparison of resistance signal outputs between deformed and undeformed CNTs/CB@AUA-SIS during detection. The error bars show the s.d. values for the results from three samples. c) The minimum detected concentration of the sensor. d) Sensitivity of the sensor when detecting petroleum ether atmospheres of different concentrations. The error bars show the s.d. values for the results from three samples. e) Resistance signal output under different vapor concentrations. f) The resistance of the sensor in response to switched petroleum ether vapor and air in 10 cycles. g) Time-dependent resistance changed during the shape recovery process of the CNTs/CB@AUA-SIS under petroleum ether vapor at a concentration of 2 g·L^{-1}.

solution underwent sonication at a power level of 60 W for 30 min. After sonication, the mixture was stirred at 200 rpm for 5 h, followed by the aforementioned curing step to prepare the sample.

Characterization: The chemical compositions of the prepared samples were measured by a Fourier transform infrared (FT-IR) spectrometer (IRTracer-100, Shimadzu) at RT in reflective mode. All spectra were scanned by acquiring 32 scans from 4000 to 400 cm^{-1}.

Tension experiments on specimens with a gauge length of 20 mm and a cross-section of 5 mm × 0.5 mm were conducted using a microcomputer-controlled electronic universal testing machine (LE3153, Lishi) at a tensile rate of 0.3 $\text{mm}\bullet\text{s}^{-1}$.

The thermal stability of the material is tested by the thermal analysis system (TGA/DSC 1, METTLER TOLEDO). The samples were heated from 30 to 600 °C at a heating rate of 5 $°\text{C}\bullet\text{min}^{-1}$ under nitrogen vapor.

The damping properties were evaluated using a dynamic mechanical analyzer (DMA242E, NETZSCH). Samples with dimensions of 20 mm × 5 mm × 0.5 mm were tested at a frequency of 1 Hz and an amplitude of 10 µm. The temperature was first equilibrated at 0 °C for 5 min and then gradually increased to 200 °C at a heating rate of 5 $°\text{C}\bullet\text{min}^{-1}$.

The shape memory properties of the AUA-SIS and composite AUA-SIS were evaluated using a dynamic mechanical analyzer (Q850 DMA, TA Instruments). To characterize the shape memory properties, the sample was initially heated to 90 °C and subjected to a compressive strain (ϵ_1). It was then cooled to 25 °C, allowing the stress to be released, resulting in a fixity strain (ϵ_2). The sample was subsequently reheated to 90 °C, and the compressive strain was restored to ϵ_3. The shape fixity ratio (R_f) and the shape recovery ratio (R_r) were defined as follows:

$$R_\text{f} = \frac{\varepsilon_2}{\varepsilon_1} \times 100\% \tag{2}$$

$$R_\text{r} = \frac{\varepsilon_1 - \varepsilon_3}{\varepsilon_1} \times 100\% \tag{3}$$

The thermal conductivity of the samples was measured using a laser flash apparatus (LFA 467 HyperFlash, NETZSCH). The samples, with a diameter of 12.7 mm, were subjected to the test to determine their thermal conductivity properties.

The morphological characterization of the samples was performed using a field emission scanning electron microscope (MIRA3, TESCAN) with an accelerating voltage of 10 kV, along with a laser confocal microscope (VK-X1000, KEYENCE).

For petroleum ether vapor, the corresponding amount of liquid was dropped into the chamber, followed by volatilization, and the vapor concentration was derived by the formula of $\frac{M}{V}$, where V is the volume of the measurement chamber, M is the mass of liquid.

The CNTs/CB@AUA-SIS samples were dimensioned to 20 mm × 5 mm × 0.5 mm for the real-time electrical monitoring test. Silver wires were employed as electrodes affixed to the samples using silver paste. Through conductive wires, the samples were connected to a resistance tester (LinkZill 01RC, LinkZill Technology). The samples were positioned in a glass container filled with petroleum ether, ensuring they did not come into direct contact with the solvent. The concentration of solvent vapor within the container was varied by adjusting the amount of petroleum ether.

The detection limit was recorded as the minimum vapor concentration that induced a discernible change in the sensor signal. The sensitivity was calculated as the ratio of changes in electrical signals ($\Delta R/R$) to changes in vapor concentration. The sensitivity of the sensor can be expressed as $\frac{\delta(\Delta R/R)}{\delta C}$, where R is the initial resistance before exposure, ΔR is the relative change in resistance, C is the vapor concentration, and δC is the change in concentration.

Supporting Information

Supporting Information is available from the Wiley Online Library or from the author.

Acknowledgements

Q.Z. and L.Z. contributed equally to this work. The work was funded by the Natural Science Foundation of Guangdong Province (2023A1515012835), the Basic Research Program of Shenzhen (JCYJ20230807093559046), and the National Natural Science Foundation of China (NFSC20240368, 52103301).

Conflict of Interest

The authors declare no conflict of interest.

Data Availability Statement

The data that support the findings of this study are available from the corresponding author upon reasonable request.

Keywords

dual-mode sensing, multi-solvent responsive, rapid responsive, shape memory polymers, vapor responsive

Received: July 30, 2025
Revised: September 12, 2025
Published online: October 3, 2025

---

[1] J. Meurer, R. H. Kampes, T. Bätz, J. Hniopek, O. Müschke, J. Kimmig, S. Zechel, M. Schmitt, J. Popp, M. D. Hager, U. S. Schubert, *Adv. Funct. Mater.* **2022**, *32*, 2207313.
[2] H. Liu, F. Wang, W. Wu, X. Dong, L. Sang, *Composites, Part B* **2023**, *248*, 110382.
[3] Y. Cui, D. Li, C. Gong, C. Chang, *ACS Nano* **2021**, *15*, 13712.
[4] Q. Kong, Y. Tan, H. Zhang, T. Zhu, Y. Li, Y. Xing, X. Wang, *Adv. Sci.* **2024**, *11*, 2407596.
[5] J. Huang, L. Qiu, C. Ni, G. Chen, Q. Zhao, *Adv. Mater.* **2024**, *36*, 2408324.
[6] H. Guo, R. Puttreddy, T. Salminen, A. Lends, K. Jaudzems, H. Zeng, A. Priimagi, *Nat. Commun.* **2022**, *13*, 7436.
[7] Y. Xia, Y. He, F. Zhang, Y. Liu, J. Leng, *Adv. Mater.* **2021**, *33*, 2000713.
[8] C. Ni, D. Chen, Y. Yin, X. Wen, X. Chen, C. Yang, G. Chen, Z. Sun, J. Wen, Y. Jiao, C. Wang, N. Wang, X. Kong, S. Deng, Y. Shen, R. Xiao, X. Jin, J. Li, X. Kong, Q. Zhao, T. Xie, *Nature* **2023**, *622*, 748.
[9] S. Zhang, C. Li, *Adv. Funct. Mater.* **2024**, *35*, 2416599.
[10] Y. Tan, Z. Liu, Z. Liu, J. Jiang, G. Li, *Chem. Eng. J.* **2023**, *454*, 140270.
[11] W. Lu, X. Le, J. Zhang, Y. Huang, T. Chen, *Chem. Soc. Rev.* **2017**, *46*, 1284.
[12] M. Ma, L. Guo, D. G. Anderson, R. Langer, *Science* **2013**, *339*, 186.
[13] W. Liu, A. Wang, R. Yang, H. Wu, S. Shao, J. Chen, Y. Ma, Z. Li, Y. Wang, X. He, J. Li, H. Tan, Q. Fu, *Adv. Mater.* **2022**, *34*, 2201914.
[14] Y. Qiu, J. Xi, Q. Wanyan, D. Wu, *ACS Appl. Polym. Mater* **2020**, *2*, 1672.
[15] H. Lu, Y. Liu, J. Leng, S. Du, *Smart Mater. Struct.* **2009**, *18*, 085003.
[16] S. Ming, Z. Li, J. Wang, H. Zhang, J. Zhao, *Chem. Eng. J.* **2024**, *479*, 147623.
[17] H. C. Wong, Q. Wang, E. M. Speller, Z. Li, J. T. Cabral, H. Y. Low, *ACS Nano* **2020**, *14*, 11352.
[18] E. Korczeniewski, P. Bryk, P. Kowalczyk, A. Z. Wilczewska, S. Boncel, R. Jedrysiak, M. Swidzinski, S. Al-Gharabli, E. Olewnik-Kruszkowska, J. Kujawa, A. P. Terzyk, *Chem. Eng. J.* **2024**, *482*, 148777.
[19] S. Basak, A. Bandyopadhyay, *Macromol. Chem. Phys.* **2021**, *222*, 2100195.

[20] N.-J. Jo, D.-H. Lim, G.-M. Bark, H.-H. Chun, I.-W. Lee, H. Park, *J. Mater. Sci. Technol.* **2010**, *26*, 763.
[21] C. Song, Y. Zhang, J. Bao, Z. Wang, L. Zhang, J. Sun, R. Lan, Z. Yu, S. Zhu, H. Yang, *Adv. Funct. Mater.* **2023**, *33*, 2213771.
[22] X. Qi, X. Yao, S. Deng, T. Zhou, Q. Fu, *J. Mater. Chem. A* **2014**, *2*, 2240.
[23] L. Xu, S. Gao, Q. Guo, C. Wang, Y. Qiao, D. Qiu, *Adv. Mater.* **2020**, *32*, 2004579.
[24] S. Liu, Y. Jing, G. Liu, *Polymers* **2024**, *16*, 892.
[25] C. Gao, M. Guo, Y. Liu, D. Zhang, F. Gao, L. Sun, J. Li, X. Chen, M. Terrones, Y. Wang, *Carbon* **2023**, *212*, 118133.
[26] Y. Huang, Y. Wang, X. Sun, X. Guo, Y. Zhang, Z. Wang, P. Liu, C. Liu, J. Qiu, Y. Zhang, *Smart Mater. Struct.* **2020**, *29*, 045014.
[27] M. Zhang, Y. Xin, *Appl. Sci.* **2020**, *10*, 723.
[28] H. Zhang, G. Zhang, M. Tang, L. Zhou, J. Li, X. Fan, X. Shi, J. Qin, *Chem. Eng. J.* **2018**, *353*, 381.
[29] W. Zhang, X. Deng, G. Sui, X. Yang, *Carbon* **2019**, *145*, 629.
[30] A. Karim, *Polymer* **2000**, *41*, 8455.
[31] Y. Li, D. Wang, J. Wen, J. Liu, D. Zhang, J. Li, H. Chu, *Adv. Funct. Mater.* **2021**, *31*, 2011259.
[32] Z. Tang, G. Deng, P. Cao, J. Gong, J. Yang, Z. Yang, Y. Sun, L. Tao, T. Wang, Q. Wang, Y. Zhang, *ACS Appl. Mater. Interfaces* **2023**, *15*, 24968.
[33] S. Wang, D. Zhang, J. Zhou, X. He, S. Y. Zheng, J. Yang, *Nano Energy* **2024**, *120*, 109166.
[34] Z. Fang, Y. Kuang, P. Zhou, S. Ming, P. Zhu, Y. Liu, H. Ning, G. Chen, *ACS Appl. Mater. Interfaces* **2017**, *9*, 5495.
[35] B. Liu, H. Li, F. Meng, Z. Xu, L. Hao, Y. Yao, H. Zhu, C. Wang, J. Wu, S. Bian, W. W. Lu, W. Liu, H. Pan, X. Zhao, *Nat. Commun.* **2024**, *15*, 1587.
[36] S. Shi, M. Cui, F. Sun, K. Zhu, M. I. Iqbal, X. Chen, B. Fei, R. K. Y. Li, Q. Xia, J. Hu, *Adv. Mater.* **2021**, *33*, 2101005.
[37] H. Yang, H. Lu, Y. Miao, Y. Cong, Y. Ke, J. Wang, H. Yang, J. Fu, *Chem. Eng. J.* **2022**, *450*, 138346.
[38] H. Du, J. Zhang, *Soft Matter* **2010**, *6*, 3370.
[39] S. T. R. Velasquez, D. Jang, P. Jenkins, P. Liu, L. Yang, L. T. J. Korley, N. Bruns, *Adv. Funct. Mater.* **2022**, *32*, 2207317.
[40] M. Chae, D. Lee, H. Kim, *Adv. Funct. Mater.* **2024**, *34*, 2405260.